

Theoretical analysis of influence of random alloy fluctuations on the opto-electronic properties of site-controlled (111)-oriented InGaAs/GaAs quantum dots

R. Benchamekh,¹ S. Schulz,¹ and E. P. O'Reilly^{1,2}

¹*Tyndall National Institute, Lee Maltings, Dyke Parade, Cork, Ireland*

²*Department of Physics, University College Cork, Cork, Ireland*

(Dated: April 5, 2022)

We use an $sp^3d^5s^*$ tight-binding model to investigate the electronic and optical properties of realistic site-controlled (111)-oriented InGaAs/GaAs quantum dots. Special attention is paid to the impact of random alloy fluctuations on key factors that determine the fine-structure splitting in these systems. Using a pure InAs/GaAs quantum dot as a reference system, we show that the combination of spin-orbit coupling and biaxial strain effects can lead to sizeable spin-splitting effects in these systems. Then, a realistic alloyed InGaAs/GaAs quantum dot with 25% InAs content is studied. Our analysis reveals that the impact of random alloy fluctuations on the electronic and optical properties of (111)-oriented InGaAs/GaAs quantum dots reduces strongly as the lateral size of the dot increases and approaches realistic sizes. For instance the optical matrix element shows an almost vanishing anisotropy in the (111)-growth plane. Furthermore, conduction and valence band mixing effects in the system under consideration are strongly reduced compared to standard (100)-oriented InGaAs/GaAs systems. All these factors strongly indicate a reduced fine structure splitting in site-controlled (111)-oriented InGaAs/GaAs quantum dots. Thus, we conclude that quantum dots with realistic (50-80 nm) base length represent promising candidates for polarization entangled photon generation, consistent with recent experimental data.

I. INTRODUCTION

Much effort from the scientific community is dedicated to the design of quantum information devices using non-classical light emitters. One of the main challenges towards achieving quantum information applications is the realization of on demand entangled photon sources.^{1,2} Semiconductor quantum dots (QDs) offer the possibility to generate polarization entangled photons via a biexciton-exciton cascade.^{3,4} Zinc-blende (ZB) InAs-based QDs grown along the [001]-direction, due to their well established growth procedures, have attracted significant interest for these kind of applications.^{2,5} However, in these systems the degenerate bright excitonic ground states in an ideal QD are split by the so-called fine-structure splitting (FSS) preventing therefore entangled photon emission. This FSS arises from the underlying C_{2v} symmetry of the combined system of QD geometry and ZB crystal structure.^{6,7} Several different approaches, such as applying external electric or strain fields, have been discussed in the literature to reduce or ideally eliminate the FSS.^{5,8-11} Of particular interest to this study, a vanishing FSS can be achieved by growing ZB-based QDs along the [111]-direction, since in this case the system has ideally C_{3v} symmetry.¹²⁻¹⁴ It has been shown both in theory^{12,13,15} and experiment^{14,16,17} that InGaAs/GaAs QDs grown along the [111]-direction are promising candidates to achieve entangled-photon emission. Despite the incontestable importance of these devices, there is a lack of detailed theoretical investigation on realistically sized and shaped (111)-oriented InGaAs QD systems. Indeed, previous theoretical studies are mainly related to model systems with dot geometries and dimensions carried over from the (001)-oriented systems. However, the geometric dimensions and shape of these site-

controlled (111)-oriented InGaAs-based QDs are very different from the structures assumed in previous theoretical studies.^{12,13} Site-controlled InGaAs/GaAs QDs exhibit typically a base length of 50-80 nm and a height of approximately 2 nm.¹⁸ This raises the question how these very different geometrical features affect the electronic and optical properties of (111)-oriented site-controlled InGaAs/GaAs QDs.

Experimental studies on site-controlled (111)-oriented InGaAs/GaAs QDs have demonstrated the generation of polarization entangled photons.^{14,16} Due to their high structural uniformity and spectral purity,¹⁹ these systems are of particular interest for device design. Moreover, experimental studies reveal that these dots seem to be very robust against composition fluctuations, since a very high percentage of the dots in the samples investigated emit entangled photons.¹⁴ This asks for a detailed atomistic analysis of the experimentally relevant site-controlled InGaAs/GaAs QDs to shed more light on the underlying physics which enables robust entangled photon generation. However, so far no such theoretical study on realistic (111)-oriented InGaAs/GaAs QDs has been presented.

Theoretical studies addressing the electronic and optical properties of realistic site-controlled structures use mainly continuum-based $\mathbf{k}\cdot\mathbf{p}$ models.²⁰ These approaches allow for insights into the general electronic and optical properties of these structures but neglect atomistic effects arising for example from random alloy fluctuations. It has been shown that in (001)-oriented InGaAs/GaAs QDs, alloy fluctuations can have a significant effect on the electronic structure, especially when studying the FSS.⁷ However, since the site-controlled QDs considered here are grown along a different crystallographic direction plus they have much larger base length than standard

(001)-oriented Stranski-Krastanov InGaAs/GaAs QDs, it is not immediately clear how alloy fluctuations will affect the electronic structure of realistic site-controlled InGaAs/GaAs (111)-oriented QDs. We show here that the geometric features, such as dot size and aspect ratio, significantly impact electronic and optical properties of site-controlled (111)-oriented InGaAs/GaAs QDs. This is especially true for key factors that affect the magnitude of the FSS. In fact our analysis reveals that the dot dimensions are critical for achieving entangled photon emission from these structures. Our analysis also highlights that the properties of (111)-oriented site-controlled dots are very different from standard (001)-oriented systems or (111)-oriented structures using geometries and dot sizes carried over from previous (001)-plane analysis.

We present here a detailed atomistic $sp^3d^5s^*$ tight-binding (TB) analysis to investigate the key factors that enable the generation of entangled photons from a high fraction of the site-controlled QDs investigated in Ref. 14. We calculate that the impact of alloy fluctuations decreases with increasing dot base size both for electrons and for holes, while the low dot height leads to the electron being only weakly confined in the dot, with a wave function which then has predominantly GaAs character. In fact we find a strong asymmetry in the number of bound electron and hole states. A detailed investigation of how different contributions, namely strain field, first- and second-order piezoelectricity and spin-orbit coupling effects, impact the properties of the QD system under consideration is presented. We find that the mixing between valence and conduction states also decreases significantly with increasing dot base length, thereby significantly reducing the size of several terms that can contribute to a finite FSS.²¹ The electron p -state splitting (*i.e.* the splitting between the first and second excited electron state) has previously been used as an indication of the ability of a given system to generate polarization entangled photons. In (001)-oriented InAs/GaAs QDs, even in the absence of alloy fluctuations, the underlying atomistic symmetry of the system leads to the situation that the electron p -states are no longer degenerate. Strain and piezoelectric effects usually increase the splitting of the p -states.²² Thus, for (001)-oriented InGaAs/GaAs QD systems, the p -state splitting arises mainly due to geometrical effects (lack of inversion symmetry due to dot geometries). In this work we consider both p -state splitting and the anisotropy of the in-plane optical momentum matrix element E_p between the electron and hole ground states as a measure of the symmetry reduction of the QDs due to random alloy fluctuations.

Even though the FSS provide a direct measure of the ability to generate polarization entangled photons, we highlight here the challenges and difficulties of carrying out an FSS calculation using the TB method for realistic site-controlled (111)-oriented InGaAs/GaAs QDs. This originates in particular from the small number of bound electron and hole states arising from the geometrical features of (111)-oriented site-controlled InGaAs/GaAs

QDs.

Our results show that while the in-plane optical momentum matrix element is perfectly isotropic for a pure InAs/GaAs QD, the p -state splitting does not vanish even when neglecting strain and built-in potential effects. We show here that this feature originates from spin-orbit coupling effects. This is a very different effect when compared to (001)-oriented InGaAs/GaAs QDs where geometrical aspects are important, as discussed above. In the case of an alloyed InGaAs/GaAs QD, the random alloy fluctuations increase the p -state splitting and cause an anisotropy of the optical momentum matrix element. Our results reveal that the impact of random alloy fluctuations on the electronic structure decreases as the lateral size of the QDs increases and that for realistic site-controlled (111)-oriented InGaAs/GaAs QDs the anisotropy of the optical momentum matrix element is negligible and the p -state splitting is mainly determined by spin-splitting effects. We conclude that the combination of all of these factors then leads to site-controlled (111)-oriented InGaAs/GaAs QDs with large base length and low dot height being particularly promising candidates for devices delivering entangled-photon emission on demand.

This paper is organized as follows. The details of the supporting theoretical framework are discussed in Sec. II. We review in Sec. III available experimental literature data on the structural properties of site-controlled (111)-oriented InGaAs/GaAs QDs and discuss how this data is incorporated in our theoretical framework. Our results are presented in Sec. IV, where we undertake a complete analysis of a (111)-oriented InGaAs/GaAs model system to study the impact of different contributions, namely the spin-orbit coupling, strain effects, built-in fields and random alloy fluctuations on the electronic structure. Finally, we summarize our results in Sec. V.

II. THEORY

In this section, we introduce the theoretical framework applied here to describe the electronic structure of site-controlled (111)-oriented InGaAs/GaAs QDs. The generation of the underlying atomistic grid for a (111)-oriented ZB system is presented in Sec. II A. The applied valence force field (VFF) model, to obtain the relaxed atomic position in a mixed InAs and GaAs system, is discussed in Sec. II B, followed by the calculation of the arising first- and second-order piezoelectric built-in potentials (Sec. II C). Subsequently, in Sec. II D, we focus on the $sp^3d^5s^*$ TB model that forms the basis of our electronic structure calculations.

A. Supercell

Since we are using an atomistic approach to describe the electronic properties of site-controlled (111)-oriented

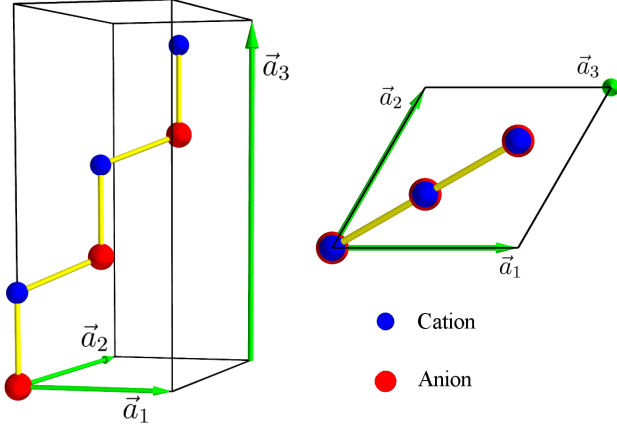


FIG. 1. Perspective view (left) and top view (right) of the six atom unit cell.

InGaAs/GaAs QDs, the grid underlying our calculations must reflect the atomic arrangement along this direction. This can be achieved by considering a unit cell of a ZB material defined by the lattice vectors:

$$\begin{aligned}
 \mathbf{a}_1 &= \left(-\frac{1}{2}, \frac{1}{2}, 0\right)a_0 \\
 \mathbf{a}_2 &= \left(-\frac{1}{2}, 0, \frac{1}{2}\right)a_0 \\
 \mathbf{a}_3 &= (1, 1, 1)a_0 .
 \end{aligned}$$

Here, a_0 is the lattice constant of the barrier material, in our case GaAs. In doing so we account for the C_{3v} symmetry of the ZB lattice when oriented along the [111]-direction. The unit cell contains six atoms (three anions $\{A\}_{i=1,\dots,3}$ and three cations $\{C\}_{i=1,\dots,3}$) placed at:

$$\begin{aligned}
 A_1 &= (0, 0, 0); & C_1 &= \left(\frac{1}{4}, \frac{1}{4}, \frac{1}{4}\right) \\
 A_2 &= \left(0, \frac{1}{2}, \frac{1}{2}\right); & C_2 &= \left(\frac{1}{4}, \frac{3}{4}, \frac{3}{4}\right) \\
 A_3 &= (0, 1, 1); & C_3 &= \left(\frac{1}{4}, \frac{5}{4}, \frac{5}{4}\right).
 \end{aligned}$$

Translating the unit cell by the vectors:

$$\begin{aligned}
 \mathbf{T}_{ijk} &= i \mathbf{a}_1 + j \mathbf{a}_2 + k \mathbf{a}_3; \\
 0 &\leq i \leq N_1, 0 \leq j \leq N_2, 0 \leq k \leq N_3,
 \end{aligned}$$

allows us to construct a supercell (SC) of a (111)-oriented ZB lattice. A schematic illustration of the SC is displayed in Fig. 1. Thus we obtain a matrix of GaAs defined by the lattice vectors $\mathbf{b}_i = N_i \mathbf{a}_i, i = 1, 2, 3$. Note that the vectors and atomic positions are expressed in the conventional coordinate system. All following expression are therefore also given in the standard (001)-oriented frame. Choosing $N_2 = N_1$, the lateral dimension of the SC is $l = N_1 a_0 / \sqrt{2}$ while its height is given by $h = N_3 a_0 \sqrt{3}$.

B. Valence force field model

The difference in the lattice constants between InAs and GaAs gives rise to a strain field in the nanostructure. This strain field corresponds to a displacement of

the atoms from their equilibrium positions. To find the relaxed atomic positions in the SC, we use the Keating VFF model.²³ In this model the total energy of an atom i is given by:

$$\begin{aligned}
 U_i &= \sum_j^N \frac{3\alpha_{ij}}{16d_{ij}^2} [\mathbf{r}_{ij}^2 - d_{ij}^2]^2 \\
 &+ \sum_{j,k>j}^N \frac{3\beta_{ijk}}{16d_{ij}d_{ik}} \left[\mathbf{r}_{ij} \cdot \mathbf{r}_{ik} + \frac{d_{ij}d_{ik}}{3} \right]^2,
 \end{aligned} \quad (1)$$

where \mathbf{r}_{ij} is the vector between the atoms i and j , and d_{ij} is the bond length between atoms i and j . Bond stretching and bending constants are denoted by α_{ij} and β_{ijk} , respectively. The parameters for α_{ij} and β_{ijk} are chosen to fit the macroscopic elastic constants C_{11} and C_{12} of GaAs and InAs.²⁴ The total energy of the system is minimized with respect to the atomic coordinates, yielding the new and relaxed atomic positions of the atoms in the SC. In and around the nanostructure, the relaxed atomic positions deviate slightly from their equilibrium positions, inducing therefore local deformations. These local strain effects lead also to the appearance of piezoelectric built-in fields in InGaAs heterostructures. We discuss the calculation of the built-in potential on our irregular atomistic grid in the next section.

C. Piezoelectric potential

Depending on the crystal structure, semiconductor materials can exhibit an electric polarization.^{25,26} This electric polarization can be divided into strain independent (spontaneous) and strain dependent (piezoelectric) contributions.²⁵ ZB semiconductors exhibit only strain dependent piezoelectric polarization fields.²⁵ In an (001)-oriented ZB case, the piezoelectric polarization vector field is connected to shear strain contributions.^{27,28} It has been shown by several authors that these piezoelectric fields are important for a realistic modeling of the electronic and optical properties of a [111]-grown ZB nanostructure.^{27,29–35} In (001)-oriented ZB materials, first- and second-order piezoelectric polarization vector fields $\mathbf{P}_{\text{pz}}^{\text{FO}}$ and $\mathbf{P}_{\text{pz}}^{\text{SO}}$, respectively, are given by:^{28,36–38}

$$\begin{aligned}
 \mathbf{P}_{\text{pz}}^{\text{FO}} &= 2e_{14} \begin{pmatrix} \epsilon_{yz} \\ \epsilon_{xz} \\ \epsilon_{xy} \end{pmatrix}, \\
 \mathbf{P}_{\text{pz}}^{\text{SO}} &= 2A_1 \begin{pmatrix} \text{Tr}(\epsilon)\epsilon_{yz} \\ \text{Tr}(\epsilon)\epsilon_{xz} \\ \text{Tr}(\epsilon)\epsilon_{xy} \end{pmatrix} + 2A_2 \begin{pmatrix} \epsilon_{B,x}\epsilon_{yz} \\ \epsilon_{B,y}\epsilon_{xz} \\ \epsilon_{B,z}\epsilon_{xy} \end{pmatrix} \\
 &+ 4B_{156} \begin{pmatrix} \epsilon_{xy}\epsilon_{xz} \\ \epsilon_{yz}\epsilon_{xy} \\ \epsilon_{yz}\epsilon_{xz} \end{pmatrix}.
 \end{aligned} \quad (2)$$

The first-order piezoelectric coefficient is denoted by e_{14} , while $A_1 = \frac{1}{3}B_{114} + \frac{2}{3}B_{124}$, $A_2 = \frac{2}{3}B_{114} - \frac{2}{3}B_{124}$ and B_{156} are the second-order piezoelectric coefficient. B_{114} , B_{124} and B_{156} are the three independent elements of the second-order piezoelectric tensor $B_{i\alpha\beta}$.²⁶

The trace of the strain tensor ϵ is denoted by $Tr(\epsilon)$ while $\epsilon_{B,i} = \frac{3}{2}\epsilon_{ii} - \frac{1}{2}Tr(\epsilon)$ are the biaxial strain components ($i = x, y, z$). First- and second-order piezoelectric coefficients have been taken from Ref. 29, which are similar to the recent hybrid functional density functional theory (DFT) results of Caro *et al.*³⁹ The main difference between the two parameter sets is the value of B_{156} , which has been shown to be of secondary importance for the QD system considered here.²⁰

The charge density ρ_{pz} arising from discontinuities in the polarization $\mathbf{P}_{pz} = \mathbf{P}_{pz}^{\text{FO}} + \mathbf{P}_{pz}^{\text{SO}}$ is given by:

$$\rho_{pz}(\mathbf{r}) = -\nabla \cdot \mathbf{P}_{pz}(\mathbf{r}). \quad (3)$$

The corresponding electrostatic built-in potential V_p is obtained from solving Poisson's equation:

$$\nabla \cdot (\epsilon_0 \kappa_0(\mathbf{r}) \nabla \cdot V_p(\mathbf{r})) = -\rho_{pz}(\mathbf{r}), \quad (4)$$

where ϵ_0 is the vacuum permittivity and $\kappa_0(\mathbf{r})$ is the position dependent static dielectric constant.

To solve Eq. (4) we use a modified finite-difference method. We cannot apply the standard finite-difference method since we are dealing here with a ZB grid plus the fact that the atoms are displaced from their equilibrium positions. To calculate derivatives on this non-uniform grid we proceed in the following way. As an example we take the differential $\frac{\partial \phi}{\partial x}$, where we calculate the derivative of a quantity ϕ with respect to the direction x . Similar considerations can be made for $\frac{\partial \phi}{\partial y}$ and $\frac{\partial \phi}{\partial z}$. In an (001)-oriented ZB system, the four vectors linking a cation to its four nearest neighbor anions read:

$$\begin{aligned} \mathbf{r}_1 &= a(1/4, 1, 4, 1/4), \\ \mathbf{r}_2 &= a(-1/4, -1, 4, 1/4), \\ \mathbf{r}_3 &= a(1/4, -1, 4, -1/4), \\ \mathbf{r}_4 &= a(-1/4, 1, 4, -1/4), \end{aligned}$$

where a denotes the lattice constant. The atoms \mathbf{r}_1 and \mathbf{r}_3 are in the half space $x > 0$ while the atoms \mathbf{r}_2 and \mathbf{r}_4 are in the half space $x < 0$. Then $\frac{\partial \phi}{\partial x}$ can be expressed as:

$$\frac{\partial \phi}{\partial x} = \frac{[\phi(\mathbf{r}_1) + \phi(\mathbf{r}_3)]/2 - [\phi(\mathbf{r}_2) + \phi(\mathbf{r}_4)]/2}{|[\mathbf{x}_1 + \mathbf{x}_3]/2 - [\mathbf{x}_2 + \mathbf{x}_4]/2|}. \quad (5)$$

Using Eq. (5) allows us to solve Eq. (4) and thus to obtain the piezoelectric potential V_p at each atomic site. The built-in potential V_p can then be included in the TB Hamiltonian as we describe in the following section.

D. Tight-binding model

To achieve an atomistic description of the electronic structure of site-controlled (111)-oriented InGaAs/GaAs QDs we apply an $sp^3d^5s^*$ TB model. Our calculations are based on the two centre parameters of Jancu *et al.*,⁴⁰ which give excellent agreement with experimental and

TABLE I. Strain parameters used in the calculations. Notations from Ref. 43 are applied.

	GaAs	InAs
n_s	0.8490	1.0500
n_p	1.1914	0.9275
n_d	1.9580	1.6620
n_{s^*}	2.0000	2.0000
$n_{ss\sigma}$	3.3000	2.2480
$n_{sp\sigma}$	3.6100	3.7700
$n_{sd\sigma}$	2.7380	1.4080
$n_{ss^*\sigma}$	0.0000	0.0000
$n_{s^*s^*\sigma}$	0.0000	0.0000
$n_{s^*p\sigma}$	2.5640	2.1240
$n_{s^*d\sigma}$	2.0000	2.0000
$n_{pp\sigma}$	3.0070	2.6980
$n_{pp\pi}$	3.1880	3.7580
$n_{pd\sigma}$	2.2470	2.1890
$n_{pd\pi}$	1.4289	1.6069
$n_{dd\sigma}$	1.0000	2.4020
$n_{dd\pi}$	2.2500	1.2140
$n_{dd\delta}$	2.9480	2.5360
π_{001}	0.2990	0.0820
π_{111}	0.4740	0.4790
δ_{001}	0.0000	0.0000
δ_{111}	0.0000	0.0000

DFT data of the unstrained binary materials. However, we reworked the strain parameters, to reproduce the bulk deformation potentials of GaAs and InAs recommended in Ref. 24. Our parameters are summarized in Table. I. The valence band offset of 0.23 eV between unstrained InAs and GaAs is used in our calculations.^{41,42} Strain effects are included into the TB Hamiltonian following the approach given in Ref. 41, which is a generalization of earlier strain models to an arbitrary local strain tensor.⁴³⁻⁴⁶ The strain dependence of the interatomic matrix elements is included via a generalized Harrison bond length scaling law.⁴⁷ On-site strain corrections for the p and d orbitals with Γ_{15} symmetry are introduced by adding the following strain Hamiltonian:⁴¹

$$\delta \hat{H} = \begin{pmatrix} 4\lambda_1 \epsilon_{B,x} & \lambda_2 \epsilon_{xy} + \xi u_z & \lambda_2 \epsilon_{zx} + \xi u_y \\ \lambda_2 \epsilon_{xy} + \xi u_z & 4\lambda_1 \epsilon_{B,y} & \lambda_2 \epsilon_{yz} + \xi u_x \\ \lambda_2 \epsilon_{zx} + \xi u_y & \lambda_2 \epsilon_{yz} + \xi u_x & 4\lambda_1 \epsilon_{B,z} \end{pmatrix}.$$

Here, ϵ denotes the local strain tensor and \mathbf{u} the internal strain vector. For p -orbitals we use $\lambda_1 = \frac{1}{2}E_p \pi_{001}$ and $\lambda_2 = \frac{8}{3}E_p \pi_{111}$ ⁴³ while for d -orbitals $\lambda_1 = \frac{1}{2}E_d \delta_{001}$ and $\lambda_2 = \frac{8}{3}E_d \delta_{111}$;⁴³ we also use $\xi = \pm \lambda_2$, with “+” for anion and “-” for cation. The values for π_{001} , π_{111} , δ_{001} and δ_{111} are given in Table I.

We calculate the local strain tensor components ϵ_{ij} and the internal strain vector $\mathbf{u} = (u_x, u_y, u_z)$ at each lattice site following Ref. 41. As an example we consider for instance an atom C in the SC. The four nearest neighbor atoms are labeled $\{A_i\}_{i=1..4}$. We introduce two sets of vectors. The first set is denoted by $\{\mathbf{r}_i^0\}_{i=1..4}$ that describes the unstrained bond lengths from atom C to the four nearest neighbor atoms $\{A_i\}_{i=1..4}$. The second set

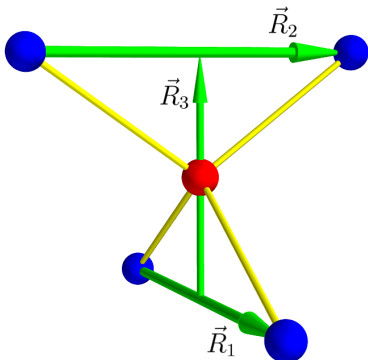


FIG. 2. Definition of the basis used in local strain field calculation.

of vectors $\{\mathbf{r}_i\}_{i=1..4}$ describes the same situation but this time after the VFF minimization/relaxation procedure. Thus $\{\mathbf{r}_i\}_{i=1..4}$ reflect the strained bond length. The centre of the tetrahedron formed by atoms A_i corresponds to the centre of a sphere that touches all vertices of the tetrahedron and its shape can be defined by three vectors $\{\mathbf{R}_i\}_{i=1..3}$ chosen as:

$$\begin{aligned}\mathbf{R}_1 &= \mathbf{r}_2 - \mathbf{r}_1, \\ \mathbf{R}_2 &= \mathbf{r}_4 - \mathbf{r}_3, \\ \mathbf{R}_3 &= 1/2(\mathbf{r}_4 + \mathbf{r}_3 - \mathbf{r}_2 - \mathbf{r}_1).\end{aligned}$$

A schematic illustration of these vectors is given in Fig. 2.

The matrix T that connects the equilibrium tetrahedron vectors $\{\mathbf{R}_i^0\}_{i=1..3}$ and the strained vectors $\{\mathbf{R}_i\}_{i=1..3}$ is calculated from:

$$T\mathbf{R}_i^0 = \mathbf{R}_i, \quad i = 1..3 \quad . \quad (6)$$

The local strain tensor ϵ for the atom C is defined by the polar decomposition:

$$T = (1 + \epsilon)P, \quad (7)$$

where P is an orthogonal matrix that rotates the unstrained tetrahedron vectors to the strained ones. The internal strain vector \mathbf{u} corresponds to the difference between the tetrahedron centre and the atom C position given after the VFF minimization scaled by the equilibrium bond length.

In addition to including strain effects into our TB model, we need also to take the piezoelectric contributions into account. We incorporate the piezoelectric potential V_p , calculated from Eq. (4), as a site-diagonal correction in the TB model. This is a widely used approach.⁴⁸⁻⁵⁰

III. SITE-CONTROLLED (111)-INGAAS/GAAS QDS: EXPERIMENTAL DATA, QD GEOMETRY AND SUPERCELL

Having presented the theoretical framework we describe here the available experimental data on the

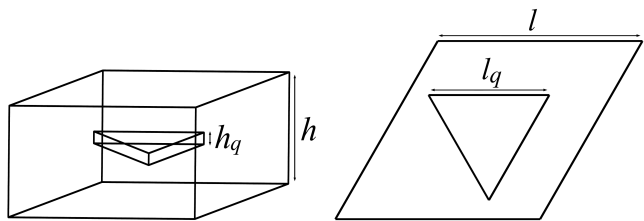


FIG. 3. Schematic perspective view (left) and top view (right) of the supercell. The base length and the height of the supercell are denoted by l and h , respectively. The QD base length is denoted by l_q while its height is given by h_q .

structural properties of site-controlled (111)-oriented InGaAs/GaAs QDs. We discuss also how their characteristic features are included in our theoretical framework.

Site-controlled (111)-oriented InGaAs/GaAs QDs, grown by metal organic vapor phase epitaxy (MOVPE) in inverted pyramidal recesses etched in a (111)-B-oriented GaAs substrate,¹⁹ exhibit a triangular shape.⁵¹⁻⁵³ The base length of the triangle is of order 50-80 nm, while the height of the nanostructure is only 1-2 nm.¹⁸ The experimentally reported InAs contents in the QDs range from 15% to 65%.⁵³

Equipped with this knowledge about the experimental data we model the QD on our atomistic grid, introduced in Sec. II A, in the following way. The QD is placed inside the GaAs matrix by substituting Ga atoms located in the QD volume by In atoms. Following the experimental findings, we assume a triangular-shaped QD. The edges of the triangular basis are along the $[\bar{1}, 1, 0]$, $[\bar{1}, 0, 1]$ and $[0, \bar{1}, 1]$ directions. A schematic illustration of the QD geometry inside the SC is shown in Fig. 3. The base length of the triangle is denoted by l_q and the height by h_q . Taking into account periodic boundary conditions, the generated SC preserves the C_{3v} symmetry of the underlying atomic grid.

For our investigation we have constructed a SC characterized by $l = 86$ nm and $h = 18$ nm (see Fig. 3). This SC contains more than 5 million atoms. We assume in the following a QD with the dimensions $h_q = 2$ nm (height) and $l_q = 55$ nm (base length), with some results also presented for QDs with a smaller base length, $l_q = 15$ nm.

IV. RESULTS

In this section we present the results of our calculations. To analyze the impact of spin-orbit coupling, strain and built-in fields on the electronic structure of the QD system in question we study in a first step a pure InAs/GaAs QD. Then we introduce random alloy fluctuations and compare the electronic structures of three different random microscopic configurations of an alloyed $\text{In}_{0.25}\text{Ga}_{0.75}\text{As}/\text{GaAs}$ QD with the results from a corresponding dot described in the virtual crystal approxima-

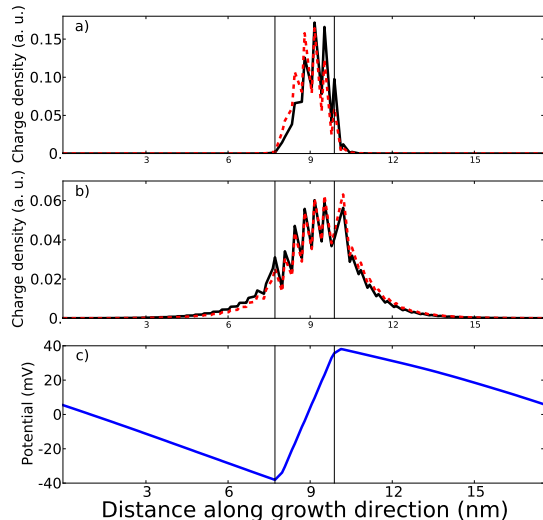


FIG. 4. a) Hole and b) electron charge densities projected along the growth direction, in the presence (solid line) and in the absence (dotted line) of the built-in potential. The profile of the piezoelectric potential along the growth direction and across the centre of a pure InAs/GaAs QD is shown in c).

tion (VCA). We also investigate the impact of dot base length by comparing the optical properties of a 25% InAs QDs with $l_q = 15$ and 55 nm.

A. Pure InAs/GaAs QD

To gain detailed understanding of the electronic structure of site-controlled InGaAs/GaAs QDs, we start with a pure system and study spin-orbit coupling, strain and built-in fields separately. The QD dimensions are $l_q = 55$ nm and $h_q = 2$ nm. Since the constructed SC should preserve the C_{3v} symmetry of the system (QD geometry plus underlying ZB lattice), we expect that for example the electron p -states should remain degenerate when including all effects other than spin-orbit coupling. The results of our analysis are summarized in Table II.

In a first step we neglect strain, built-in field and spin-orbit coupling and focus purely on quantum confinement (QC) effects. Our results confirm the expected degeneracy of the electron and hole p -states. In a next step, we introduce strain effects by relaxing the atomic positions using the VFF model described in Sec. II B. We still neglect spin-orbit coupling and built-in field effects. Our calculations show that when including strain effects the hole and electron ground states are shifted to higher energies due to the presence of hydrostatic and biaxial compressive strains. We note also that in this particular case where spin-orbit coupling is neglected, including strain switches the order of the s - and p -shell in the valence band. The electron and hole p -states are still degener-

TABLE II. Energy gap (E_g), the hole s - and p -shell state energies (E_h^s and E_h^p) and the electron s - and p -shell state energies (E_e^s and E_e^p) for a pure InAs/GaAs QD ($l_q = 55$ nm, $h_q = 2$ nm) calculated without spin-orbit coupling, considering only the quantum confinement (QC), the quantum confinement and the strain (QC+ ϵ), and the quantum confinement, the strain and the built-in potential (QC+ ϵ +PZ). The energies (in meV) are given with respect to the bulk GaAs valence band maximum.

	QC	QC+ ϵ	QC+ ϵ +PZ
E_g	992.3	1089.6	1090.2
E_h^s	171.1	407.1	392.
E_h^p	170.6	408.6	392.6
E_e^s	1163.4	1497.7	1482.8
E_e^p	1175.8	1510.0	1492.0

ate. Next, we include the total (first- plus second-order) piezoelectric potential in the calculations. The piezoelectric potential increases the calculated energy gap between the highest hole and the electron state by 1.1 meV. This is initially surprising, as one normally expects for a symmetric dot that a potential variation such as that in Fig. 4(c) will reduce both the electron and hole confinement energies (quantum confined Stark effect). The anomalous behaviour observed in this case can however be understood from Figs. 4(a) and (b), which show that both the electron and hole wavefunctions are shifted towards the top of the dot. This asymmetry in the electron and hole wavefunctions would not be predicted using a continuum model to describe the electronic structure, but arises here as a natural consequence of the underlying atomic structure of the (111)-oriented dot.

Table II summarizes also the energy gap and the electron and hole s - and p -shell energies without spin-orbit coupling. Please note that the p -states remain degenerate when including the piezoelectric potential. All this shows that our SC and QD geometry accurately reflects and preserves the C_{3v} symmetry. No artificial symmetry breaking is introduced.

Without the spin-orbit coupling the symmetry properties of the system were determined by geometrical symmetries. In terms of group theory, in the absence of spin-orbit coupling effects the irreducible representations of the *single* group C_{3v} are important. When including spin-orbit coupling effects one has to deal with *double* groups, in this case \bar{C}_{3v} . This group contains only two dimensional irreducible representations.⁵⁴ Consequently, each state can only be two-fold (Kramers) degenerate. Table III summarizes the energy gap (E_g), the electron p -state splitting (ΔE_p^e) between the two-fold Kramers degenerate states and the electron (E_e^0) and hole (E_h^0) ground state energies. For the unstrained QD, including the spin-orbit coupling, the p -state splittings are tiny (0.06 meV for holes and 0.04 meV for electrons). When including strain effects the p -state splittings are one order of magnitude larger (1.31 meV for holes and 0.36 meV for electrons). The effect of the piezoelectric potential on the

TABLE III. Energy gap (E_g), the two highest valence states energies (E_h^0 and E_h^1), the two lowest electron energies (E_e^0 and E_e^1) and electron and hole p -states splittings (ΔE_p^e and ΔE_p^h) for a pure InAs/GaAs QD calculated including spin-orbit coupling. The energies (in meV) are given with respect to the bulk GaAs valence band maximum.

	QC	QC+ ϵ	QC+ ϵ +PZ
E_g	872.7	980	982.4
E_h^0	182.0	407.3	397.4
E_h^1	176.6	398.9	386.9
ΔE_p^h	0.06	1.31	1.4
E_e^0	1054.7	1387.3	1379.8
E_e^1	1067.4	1399.5	1.388.7
ΔE_p^e	0.04	0.36	0.3

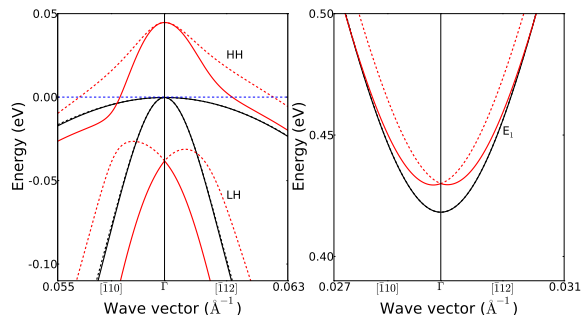


FIG. 5. Heavy and light hole (left) and lowest electron states band structure around Brillouin zone centre of bulk InAs, before (black lines) and after (red lines) applying a (111) biaxial strain of 1%.

p -state splittings is negligible (cf. Table III). In combination with our calculations without spin-orbit coupling, we have shown that spin-orbit effects are the origin of the here observed tiny p -state splitting in a triangular-shaped (111)-oriented InAs/GaAs QD and that the lattice constant mismatch between InAs and GaAs amplifies this splitting. This is a consequence of the increase of electron and hole spin splitting induced by a (111)-oriented biaxial strain. In order to confirm this statement, we show in Fig. 5 the band structure of bulk InAs before and after applying a (111)-oriented biaxial strain of 1%. Our model gives a large strain-induced spin-splitting for this particular strain type, associated with the C_5 shear-strain linear- k term in the Pikus-Bir Hamiltonian.^{55,56} We note also that the light hole state spin splitting is more sensitive to strain, this is in line with previous investigation of strain-induced spin-splitting associated with the C_4 axial-strain linear- k term.⁵⁷

It should be noted that the p -state splitting introduced by the spin-orbit coupling does not lead to a FSS. This is discussed in detail by Karlsson *et al.* (Ref. 15) in terms of group theory. Thus, in contrast to (001)-oriented InAs/GaAs QDs, where the p -state splitting is introduced mainly by strain field anisotropy or piezoelectric built-in potentials, a non-vanishing p -state splitting

in (111)-oriented InAs/GaAs QDs is not directly indicative of the presence of a FSS.

To shed more light on the electronic structure of site-controlled (111)-oriented InAs/GaAs QDs, Fig. 6 displays the charge densities of the four energetically highest valence states and the four energetically lowest conduction states when taking all the different contributions (strain, built-in fields) into account. The charge densities of Fig. 6 reflect the triangular-shaped QD confinement. It can also be seen from Figs. 4 and 6 that the holes are more localized than electrons, both along the growth direction and in the growth plane, primarily because of the larger effective masses of holes than electrons.

B. Alloyed QD

Having discussed the influence of spin-orbit coupling, strain and built-in fields on the electronic properties of site-controlled (111)-oriented InAs/GaAs QDs, we turn now and study the impact of random alloy fluctuations on their electronic and optical properties. We consider here an InAs content of 25%, which is well within the experimentally relevant range (cf. Sec. III). As a reference point for our random alloy calculations we perform in a first step a VCA calculation. In this calculation the QD region is filled with a virtual crystal for which the TB parameters, the elastic and piezoelectric constants are simply a concentration weighted average of the corresponding bulk InAs and GaAs parameters. Since we are mainly interested in investigating the robustness of the electronic structure of the QD system against alloy fluctuations, the adjustment of the VCA results by introducing bowing parameters for the involved TB parameters is beyond the scope of the present work. Obviously, using the VCA for electronic structure calculations of site-controlled $\text{In}_{0.25}\text{Ga}_{0.75}\text{As}/\text{GaAs}$ QD does not change the symmetry of the system. Therefore, in terms of the p -state splitting, similar results as for the pure InAs/GaAs QD are expected. Quantitatively, the energy gap for the 25% InAs VCA calculation is larger than in the pure InAs case, since GaAs has a larger band gap and we have less InAs content in the QD. The smaller InAs content results also in a reduced carrier confinement. Figure 7 show the charge densities of hole and electron ground states projected on the growth direction, in the presence and in the absence of the built-in potential. The profile of the piezoelectric potential along the growth direction and across the centre of the QD is also displayed in Fig. 7. As in the case of a pure InAs/GaAs QD, the wavefunctions are asymmetric with respect to the (111) mirror plane; however this asymmetry is less pronounced in the case of a virtual $\text{In}_{0.25}\text{Ga}_{0.75}\text{As}/\text{GaAs}$ QD when compared with the pure system (cf. Fig. 4). Also, we note that the piezoelectric potential profile is inverted compared to the case of a pure InAs QD (Fig. 4), where the large lattice mismatch leads to the second-order piezoelectric potential contribution being larger than the first-order one.

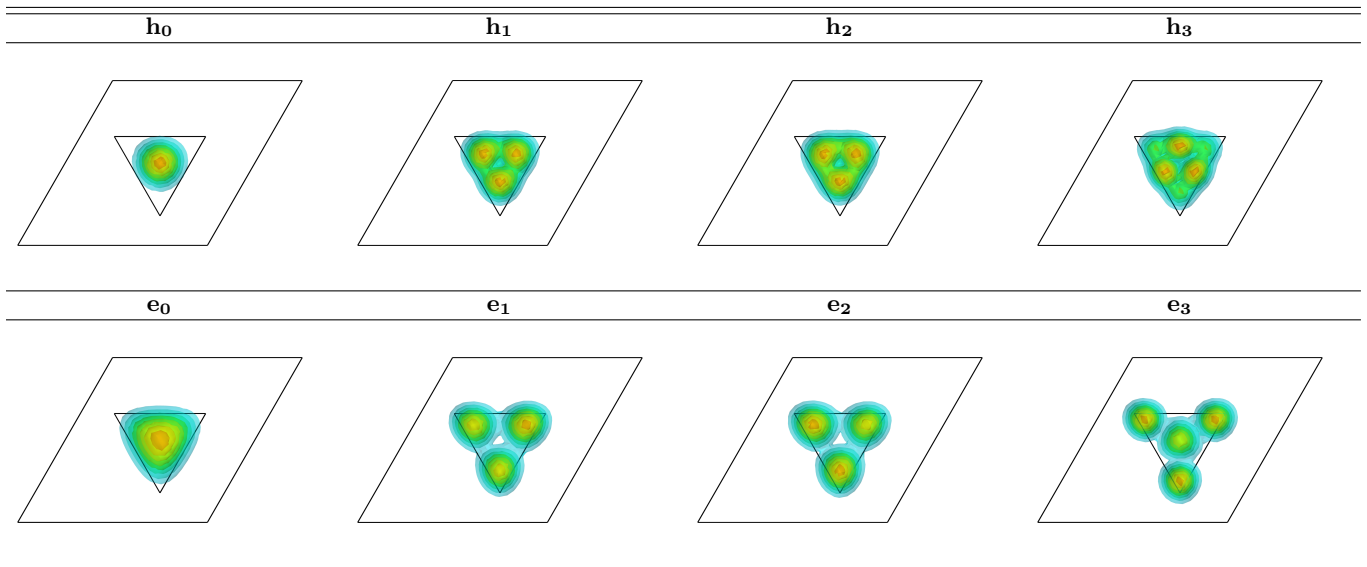


FIG. 6. Isosurfaces plot of charge densities of the four energetically highest valence states (h_0 , h_1 , h_2 , h_3) and the four energetically lowest conduction states (e_0 , e_1 , e_2 , e_3) in a triangular-shaped (111)-oriented InAs/GaAs QD.

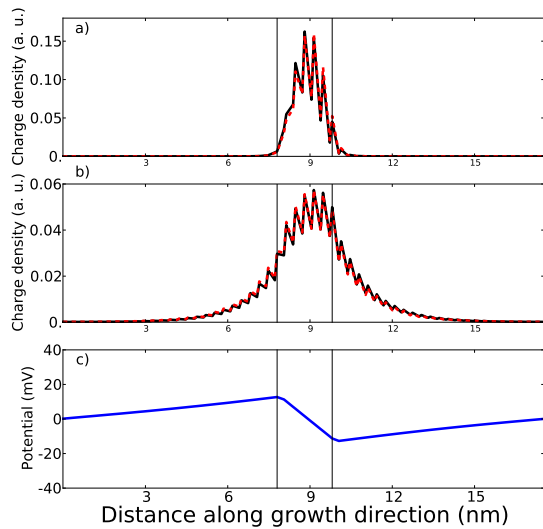


FIG. 7. Same as Fig. 4 for a $\text{In}_{0.25}\text{Ga}_{0.75}\text{As}/\text{GaAs}$ QD within VCA.

To analyze the impact of random alloy fluctuations at a microscopic level, we randomly replace Ga atoms in the QD region by In atoms so that the (111)-oriented QD contains 25% InAs. To study the influence of the alloy microstructure on the electronic and optical properties, we have constructed three different microscopic random configurations. Figure 8 shows the electron (e_0) and hole (h_0) ground state charge densities for the VCA case together with the results from the three different random configurations (Configs. 1 - 3). The charge densities obtained from the VCA calculation are symmetric with

respect to rotations of 120° around the central QD axis. This is in contrast to the results of the alloyed calculations. Here the charge densities appear deformed due to the random distribution of the In and Ga atoms inside the QD. The deformation is more pronounced for the hole states due to the larger hole effective mass compared with the electron mass, and also due to the stronger hole confinement in the QD.

The contribution of the different orbital types to the electronic wavefunctions are also presented in Fig. 8. With the Hamiltonian that we are using, the zone centre bulk valence band maximum states are made up of p and d orbitals, with the lowest conduction states having s and s^* character. As expected, the highest valence states in the QD are mainly made of p and d orbitals, with $< 0.2\%$ s and s^* conduction character. Likewise, the electron states are made of s and s^* orbitals, with $< 1\%$ valence character. This is to be compared with (001) InGaAs/GaAs QDs, which generally have a much lower base length to height ratio, and for which the results of typical calculations give 1% conduction character in the highest valence states and $\sim 10\%$ valence character in the lowest conduction state.⁵⁸ Mixing of valence and conduction states is one of the factors that can contribute to a finite FSS value.²¹ Looking at the results by Krapek *et al.*²¹ the electron-hole exchange interaction matrix elements EX , which mainly determine the magnitude of the FSS, can be expressed as a sum of three contributions $EX = EX_0 + EX_1 + EX_2$. In Ref. 21, the authors show that EX_0 and EX_1 depend on the conduction and valence band mixing contributions. Consequently, if conduction and valence bands are decoupled, for instance in a two plus six band $\mathbf{k} \cdot \mathbf{p}$ model,^{59,60} $EX_0 = EX_1 = 0$ and only EX_2 contributes. Additionally, Krapek and co-workers show that the contribution

from these three terms to the FSS scale as $EX_0 \sim 1/L$, $EX_1 \sim 1/L^2$ and $EX_2 \sim 1/L^3$, where L is the extension of the wavefunction, which is then to a good approximation proportional to the dot size. Thus the larger the QD, the smaller the contribution of the electron-hole exchange interaction and consequently the FSS. Therefore, the large aspect ratio ($\frac{l_q}{h_q} \sim 25$) of the here considered realistic site-controlled (111)-oriented InGaAs/GaAs QDs has two consequences. Firstly, the conduction-valence mixing is significantly reduced. Secondly, the magnitude of the term EX_2 is strongly reduced. All in all, this highlights again that the geometrical features of realistic site-controlled (111)-oriented InGaAs/GaAs dots lead to electronic and optical properties that are very different from standard (001)-oriented InGaAs/GaAs dot systems. Obviously all this is of benefit for achieving a high proportion of dots with minimal FSS, as reported in the literature.⁶¹ We will return to the calculation of many-body effects, such as the FSS, in more detail below. We note also that the p_x , p_y and p_z states contribute equally to the hole ground state wave function in the case of the VCA calculation, while their contributions are slightly different when including alloy fluctuations. The impact of these fluctuations on the optical properties of the QDs will be discussed further below.

Table IV summarizes the energy gap (E_g) and the electron (ΔE_p^e) and hole (ΔE_p^h) p -state splitting for the different configurations. One can infer from this table, that in terms of the variation in the energy gap (E_g), there is very little difference between the different random configurations. Thus, with a small number of random configurations one obtains already reliable insight into the physics of site-controlled (111)-oriented InGaAs/GaAs QDs. This is in stark contrast to wurtzite nitride-based alloys containing InN (such as AlInN or InGaN), where the electronic and optical properties are strongly influenced by the microscopic structure of the alloy.^{62–64} When looking at the p -state splitting, cf. Table IV, we find that all three random configurations give a splitting below 1 meV. This supports that the symmetry of realistically shaped site-controlled InGaAs/GaAs QDs is only weakly affected by random alloy fluctuations, consistent with the recent demonstration of their potential for on demand entangled photon emitters.^{14,16}

It is beyond the scope of the present study to carry out the full many-body calculations required to determine the FSS accurately; we can however give an overview here what is required and highlight the challenges of such a calculation for realistically sized and shaped (111)-oriented site-controlled InGaAs/GaAs QDs. Given the particularities of the system under consideration, approaches used for (001)-oriented systems are not directly applicable here for the following reasons. Usually, to determine the FSS, configuration interaction schemes are applied.^{7,65} This involves the calculation of Coulomb matrix elements describing the attractive electron-hole interaction as well as the electron-hole exchange interaction.^{66–68} These matrix elements are calculated from the

TABLE IV. Energy gap (E_g), the two highest hole states energies (E_h^0 and E_h^1), the two lowest electron energies (E_e^0 and E_e^1) and electron (ΔE_p^e) and hole (ΔE_p^h) p -states splittings for a triangular-shaped (111)-oriented In_{0.25}Ga_{0.75}As/GaAs QD calculated within (VCA) and for three different random alloy configurations (Config. 1, 2 and 3). The energies (in meV) are given with respect to the bulk GaAs valence band maximum.

	VCA	Config. 1	Config. 2	Config. 3
E_g	1484.5	1427.2	1427.8	1427.6
E_h^0	58.4	72.4	71.0	71.2
E_h^1	52.4	67.8	65.3	67.5
ΔE_p^h	0.48	1.3	1.0	1.9
E_e^0	1511.0	1499.6	1498.8	1498.8
E_e^1	1516.5	1504.7	1503.9	1503.6
ΔE_p^e	0.01	0.15	0.03	0.41

bound electron and hole single-particle wavefunctions. For an accurate CI calculation two main factors are important. First, to construct the many-body Hamiltonian in the basis of anti-symmetrized products of bound single-particle electron and hole states, a sufficiently large number of these bound single-particle states is required. This has been highlighted and discussed in detail by Wimmer *et al.*⁶⁹ and Schliwa *et al.*⁶⁵. For instance, the data presented in Ref. 65 shows for a (001)-oriented InGaAs/GaAs QD that at least 6 bound electron and 6 bound hole states have to be included to describe correlation effects accurately. The pseudo-potential calculations by Bester *et al.*⁷ included even more basis states, namely 12 bound electron and 12 bound hole states, to achieve an accurate value for the FSS in (001)-oriented InAs/GaAs QDs. However, this approach presents a problem for realistic site-controlled (111)-oriented InGaAs/GaAs QDs, since we have here a strong asymmetry between the bound electron and hole states. In fact we find only three weakly bound electron states. Such a small number of basis states should make it difficult to apply the standard CI approach used in (001)-oriented system in a straightforward way. For other QD systems, such as InGaN/GaN QDs similar arguments and discussions have been made.⁷⁰ One approach to circumvent problems arising from the small number of bound electron and hole states is to perform first a self-consistent Hartree-Fock calculation and use the resulting wave functions as input for CI calculations.⁷¹ Since the supercells that have to be considered for realistic site-controlled (111)-oriented InGaAs/GaAs QDs are huge (> 5 million atoms), self-consistent calculations are computationally extremely demanding.

However, leaving the issue of the small number of bound electron states aside, a further challenge that one encounters here is the accurate calculation of the Coulomb matrix elements required for the CI. For an accurate calculation of the FSS the electron-hole exchange matrix elements need in particular to be calculated accurately. These matrix elements are usually one order of

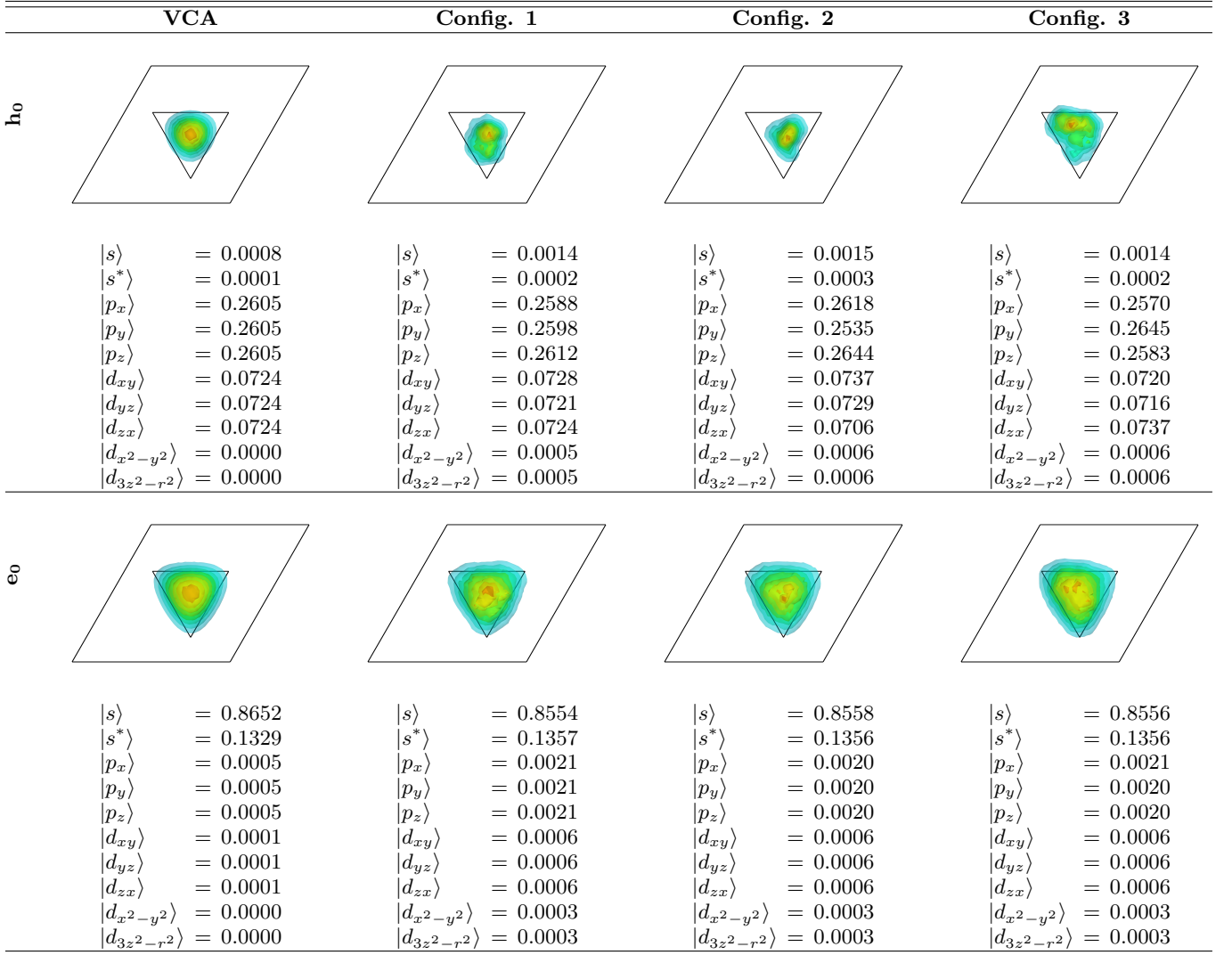


FIG. 8. Isosurfaces plot of hole (top) and electron (bottom) ground state charge densities for a triangular-shaped (111)-oriented $\text{In}_{0.25}\text{Ga}_{0.75}\text{As}/\text{GaAs}$ QD obtained within the VCA and for the three different random alloy configurations considered (Configs. 1-3). Also we show for each case what fraction of the state projects onto each type of atomic orbitals used in the $sp^3d^5s^*$ TB model.

magnitude smaller than the direct electron-hole Coulomb matrix elements.⁷² Small changes in the values of the exchange matrix elements might lead to large changes in the FSS, which is only of the order of μeV .⁷ In the framework of an empirical tight-binding model, calculations of the Coulomb matrix elements present a challenge since usually the underlying atomic-like basis states are not explicitly known.⁷³ The standard approach is to make assumptions about the atomic-like basis states (Most often Slater orbitals are used), and calculate with those states the on-site Coulomb contributions. For nearest neighbor and more distant contributions the on-site Coulomb matrix elements are scaled by $1/r$ and weighted by the tight-binding expansion coefficients.⁷² Thus the precise structure of the underlying basis states is neglected and the Coulomb interaction is treated on the length scale of lattice vectors. For the direct attractive Coulomb in-

teraction this approach has been shown to be a good approximation.⁷² However, since the electron-hole exchange terms are dominated by short range contributions, more precise knowledge about the underlying wavefunctions is required. This has been discussed in detail by Korkusinski *et al.*⁷⁴, for instance. For an accurate treatment of the electron-hole exchange terms more advanced approaches are required, which fit not only the bulk band structures but also the wave functions to DFT wave functions.⁷³ But, using such an approach in conjunction with a self-consistent Hartree-Fock calculation as input for CI calculations is beyond the scope of the present work.

Nevertheless, even without the explicit calculation of the FSS, we can gain insight into key parameters which are reliable indicators for the symmetry breaking due to random alloy effects. One of these indicators is the p -state splitting discussed above. As a further measure,

we can use the angular dependent interband transition optical matrix element, E_p^α :⁷⁵

$$E_p^\alpha = \frac{2}{m_0} p_\alpha^2. \quad (8)$$

Here p_α is the optical momentum component in the direction u_α in the (111) plane and α denotes the angle between u_α and the [110]-direction. We have used the method in Ref. 76 to calculate p_α between electron and hole ground states for two dot sizes, firstly with base length $l_q = 15$ nm, and then with $l_q = 55$ nm. For both systems the height of the dot is kept the same. Figure 9 shows E_p^α as a function of the angle α for the VCA results (solid blue line) and the three different random alloy configurations for the dot with base length $l_q = 15$ nm (Config.1: dashed green line, Config.2: dashed-dotted red line, Config.3: blue dotted line). Without alloy fluctuations E_p^α is independent of α . For the random alloy configurations we find that E_p^α depends on α . To quantify the impact of the random alloy fluctuations on the ideally circular symmetric E_p^α we introduce the following measure:

$$\beta = [\text{Max}(E_p^\alpha) - \text{Min}(E_p^\alpha)] / \text{Min}(E_p^\alpha). \quad (9)$$

The ratio β is equal to 0 for a symmetric system, i.e. a pure InAs/GaAs QD or an alloyed system treated within VCA. β measures exclusively the effect of alloy fluctuations on the QD symmetry. For the three considered configurations, β is equal to 0.060, 0.055 and 0.109, respectively. These numbers reflect and confirm the data shown in Fig. 9. This angular asymmetry in the single particle recombination properties will contribute to an increase in the FSS, reflecting that orthogonal axes in the QD now have distinct properties.

Figure 10 shows the angular dependence of E_p^α between electron and hole ground states calculated within the VCA and for three different random alloy configurations for an In_{0.25}Ga_{0.75}As/GaAs QD with the dimensions $l_q = 55$ nm and keeping unchanged the height $h_q = 2$ nm. Compared to Fig. 9, we notice a smaller anisotropy of the optical momentum matrix element, with β respectively equal to 0.006, 0.033 and 0.033, for the three different configurations considered. This is indicative that the effects of random alloy fluctuations reduce with increasing QD base size.

Overall, based on both the p -state splitting and the optical momentum matrix elements, our calculations reveal that random alloy fluctuations affect the electronic and optical properties of realistic site-controlled InGaAs/GaAs QDs only slightly. Keeping in mind that the size of the considered QDs is at the lower limit of the experimental size range (50-80 nm) and that the anisotropy in E_p^α should further reduce with increasing size, our analysis confirms that site-controlled (111)-oriented InGaAs/GaAs QDs are promising candidates as future entangled photon sources. Additionally, since the electron-hole exchange matrix elements are inversely

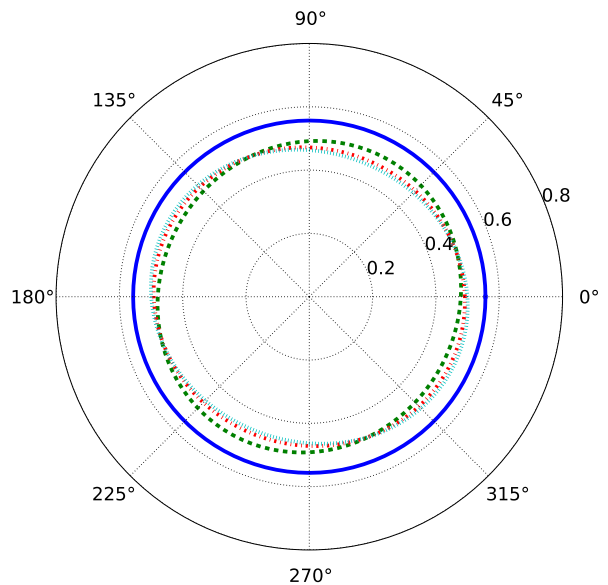


FIG. 9. Angular dependence of the in-plane optical matrix element (in eV) of a small ($l_q = 15$ nm) In_{0.25}Ga_{0.75}As/GaAs QD calculated within the VCA (solid blue line) and three different alloyed configurations (Config.1: dashed green line, Config.2: dashed-dotted red line, Config.3: blue dotted line)

proportional to the dot size, this further supports that for even larger dots, the FSS values should tend to much lower values than in standard (001)-oriented InGaAs/GaAs dots. This finding is in line with recent experimental results where an area with up to 15% of polarization-entangled photon emitters was obtained.¹⁴

V. CONCLUSION

In conclusion, we investigated the optoelectronic properties of triangular-shaped (111)-oriented InGaAs/GaAs QDs using an $sp^3d^5s^*$ TB model including local strain field and piezoelectric potential effects. Overall, we find that the electronic and optical properties of these systems are vastly different from standard (001)-oriented InGaAs/GaAs systems.

In contrast with continuum models previously used to describe realistic site-controlled (111)-oriented InGaAs/GaAs QDs, all the symmetry operations of these structures are well described by our atomistic model including the absence of the horizontal reflection plane. This is reflected in the asymmetry of the obtained charge densities. Furthermore, our atomistic description clarifies the importance of random alloy fluctuations on the electronic and optical properties of site-controlled (111)-oriented QDs which cannot be addressed by continuum-based models. We considered electron and hole p -state splittings as well as the anisotropy in the interband transition optical matrix element as measures of the C_{3v} sym-

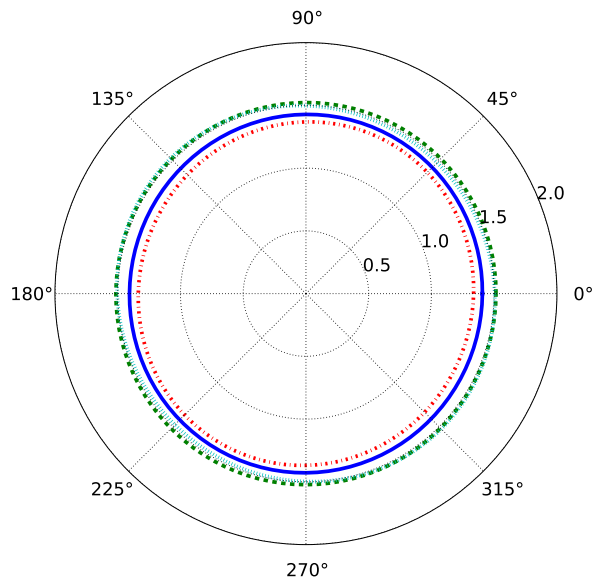


FIG. 10. Same as in Fig. 9 for a larger ($l_q = 55$ nm) $\text{In}_{0.25}\text{Ga}_{0.75}\text{As}/\text{GaAs}$ QD.

metry reduction. We show that the p -state degeneracy is lifted either by including spin-orbit coupling or by random alloy fluctuations. The value of the p -state splitting is mainly governed by the amplitude of the strain due to

the induced spin splitting in the case of realistically sized (111)-oriented $\text{InGaAs}/\text{GaAs}$ QD structures. The electron p -state splitting remains smaller than 0.2 meV for all the here considered configurations and the interband transition anisotropy becomes very small with increasing dot base size. Also we find that conduction and valence band mixing effects are strongly reduced in comparison with standard (001)-oriented $\text{InGaAs}/\text{GaAs}$ QD systems. This reduced mixing is also indicative of a reduced FSS in site-controlled (111)-oriented $\text{InGaAs}/\text{GaAs}$ QDs.²¹ Furthermore, we show that the anisotropy in E_p^α and the p -state splitting reduce with increasing the QD lateral size. Since the size of the here considered QDs is at the lower limit of the experimentally realized structures, our results indicate that the larger QDs are even more promising for achieving entangled photon generation, and support thus the potential of site-controlled (111)-oriented $\text{InGaAs}/\text{GaAs}$ QDs as polarization entangled photon emitters in future quantum information applications.

ACKNOWLEDGEMENT

This work was carried out with the financial support of Science Foundation Ireland (project number 10/IN.1/I2994). The authors would like to acknowledge the SFI/HEA Irish Center for High-End Computing for computational resources.

-
- ¹ D. Bouwmeester, A. Ekert, and A. Zeilinger, *The Physics of Quantum Information* (Springer, Berlin, 2000).
 - ² M. Müller, S. Bounouar, K. D. Jöns, M. Glässl, and P. Michler, *Nat. Photonics* **8**, 224 (2014).
 - ³ O. Benson, C. Santori, M. Pelton, and Y. Yamamoto, *Phys. Rev. Lett.* **84**, 2513 (2000).
 - ⁴ N. Akopian, N. H. Lindner, E. Poem, Y. Berlatzky, J. Avron, D. Gershoni, B. D. Gerardot, and P. M. Petroff, *Phys. Rev. Lett.* **96**, 130501 (2006).
 - ⁵ J. Plumhof, R. Trotta, A. Rastelli, and O. Schmidt, *Nanoscale Research Letters* **7**, 336 (2012).
 - ⁶ R. Seguin, A. Schliwa, S. Rodt, K. Potschke, U. W. Pohl, and D. Bimberg, *Phys. Rev. Lett.* **95**, 257402 (2005).
 - ⁷ G. Bester, S. Nair, and A. Zunger, *Phys. Rev. B* **67**, 161306(R) (2003).
 - ⁸ J.-W. Luo, R. Singh, A. Zunger, and G. Bester, *Phys. Rev. B* **86**, 161302 (2012).
 - ⁹ A. Rastelli, F. Ding, J. D. Plumhof, S. Kumar, R. Trotta, C. Deneke, A. Malachias, P. Atkinson, E. Zallo, T. Zander, A. Herklotz, R. Singh, V. Krápek, J. R. Schröter, S. Kivavittaya, M. Benyoucef, R. Hafenbrak, K. D. Jöns, D. J. Thurmer, D. Grimm, G. Bester, K. Dörr, P. Michler, and O. G. Schmidt, *physica status solidi (b)* **249**, 687 (2012).
 - ¹⁰ M. A. Pooley, A. J. Bennett, R. M. Stevenson, A. J. Shields, I. Farrer, and D. A. Ritchie, *Phys. Rev. Applied* **1**, 024002 (2014).
 - ¹¹ Y. H. Huo, B. J. Witek, S. Kumar, J. R. Cardenas, J. X. Zhang, N. Akopian, R. Singh, E. Zallo, R. Grifone, D. Kriegner, R. Trotta, F. Ding, J. Stangl, V. Zwiller, G. Bester, A. Rastelli, and O. G. Schmidt, *Nat. Physics* **10**, 46 (2014).
 - ¹² A. Schliwa, M. Winkelkemper, A. Lochmann, E. Stock, and D. Bimberg, *Phys. Rev. B* **80**, 161307 (2009).
 - ¹³ R. Singh and G. Bester, *Phys. Rev. Lett.* **103**, 063601 (2009).
 - ¹⁴ G. Juska, V. Dimastrodonato, L. O. Mereni, A. Gocalinska, and E. Pelucchi, *Nat. Photonics* **7**, 527 (2013).
 - ¹⁵ K. F. Karlsson, M. A. Dupertuis, D. Y. Oberli, E. Pelucchi, A. Rudra, P. O. Holtz, and E. Kapon, *Phys. Rev. B* **81**, 161307 (2010).
 - ¹⁶ G. Juska, E. Murray, V. Dimastrodonato, T. H. Chung, S. T. Moroni, A. Gocalinska, and E. Pelucchi, *J. Appl. Phys* **117**, 134302 (2015).
 - ¹⁷ J. Wang, M. Gong, G.-C. Guo, and L. He, *Phys. Rev. Lett.* **115**, 067401 (2015).
 - ¹⁸ S. B. Healy, R. J. Young, L. O. Mereni, V. Dimastrodonato, E. Pelucchi, and E. P. O'Reilly, *Physica E (Amsterdam)* **42**, 2761 (2010).
 - ¹⁹ L. O. Mereni, V. Dimastrodonato, R. J. Young, and E. Pelucchi, *Appl. Phys. Lett.* **94**, 223121 (2009).
 - ²⁰ O. Marquardt, E. P. O'Reilly, and S. Schulz, *J. Phys.: Condens. Matter* **26**, 035303 (2014).

- ²¹ V. Krápek, P. Klenovský, and T. Šikola, *Phys. Rev. B* **92**, 195430 (2015).
- ²² G. Bester and A. Zunger, *Phys. Rev. B* **71**, 045318 (2005).
- ²³ P. N. Keating, *Phys. Rev.* **145**, 637 (1966).
- ²⁴ I. Vurgaftman, J. R. Meyer, and L. R. Ram-Mohan, *Journal of Applied Physics* **89** (2001).
- ²⁵ J. F. Nye, *Physical Properties of Crystals: Their Representation by Tensors and Matrices* (Oxford University Press, New York, 1985).
- ²⁶ H. Grimmer, *Acta Cryst.* **A63**, 441 (2007).
- ²⁷ D. L. Smith and C. Mailhot, *Rev. Mod. Phys.* **62**, 173 (1990).
- ²⁸ Y. M. Niquet, *Phys. Rev. B* **74**, 155304 (2006).
- ²⁹ A. Beya-Wakata, P.-Y. Prodhomme, and G. Bester, *Phys. Rev. B* **84**, 195207 (2011).
- ³⁰ D. Smith, *Solid State Communications* **57**, 919 (1986).
- ³¹ D. L. Smith and C. Mailhot, *Journal of Vacuum Science & Technology A* **5**, 2060 (1987).
- ³² C. Mailhot and D. L. Smith, *Phys. Rev. B* **35**, 1242 (1987).
- ³³ D. L. Smith and C. Mailhot, *Phys. Rev. Lett.* **58**, 1264 (1987).
- ³⁴ C. Mailhot and D. L. Smith, *Journal of Vacuum Science & Technology A* **7**, 609 (1989).
- ³⁵ D. L. Smith and C. Mailhot, *Journal of Applied Physics* **63**, 2717 (1988).
- ³⁶ G. Bester, A. Zunger, X. Wu, and D. Vanderbilt, *Phys. Rev. B* **74**, 081305 (2006).
- ³⁷ A. Schliwa, M. Winkelnkemper, and D. Bimberg, *Phys. Rev. B* **76**, 205324 (2007).
- ³⁸ S. Schulz, M. A. Caro, E. P. O'Reilly, and O. Marquardt, *Phys. Rev. B* **84**, 125312 (2011).
- ³⁹ M. A. Caro, S. Schulz, and E. P. O'Reilly, *Phys. Rev. B* **91**, 075203 (2015).
- ⁴⁰ J.-M. Jancu, R. Scholz, F. Beltram, and F. Bassani, *Phys. Rev. B* **57**, 6493 (1998).
- ⁴¹ F. Raouafi, R. Benchamekh, M. O. Nestoklon, J.-M. Jancu, and P. Voisin, *Journal of Physics: Condensed Matter* **28**, 045001 (2016).
- ⁴² B. Soucail, N. Dupuis, R. Ferreira, P. Voisin, A. P. Roth, D. Morris, K. Gibb, and C. Lacelle, *Phys. Rev. B* **41**, 8568 (1990).
- ⁴³ J.-M. Jancu and P. Voisin, *Phys. Rev. B* **76**, 115202 (2007).
- ⁴⁴ Y. M. Niquet, D. Rideau, C. Tavernier, H. Jaouen, and X. Blase, *Phys. Rev. B* **79**, 245201 (2009).
- ⁴⁵ T. B. Boykin and P. Vogl, *Phys. Rev. B* **65**, 035202 (2001).
- ⁴⁶ M. Zieliński, *Phys. Rev. B* **86**, 115424 (2012).
- ⁴⁷ S. Y. Ren, J. D. Dow, and D. J. Wolford, *Phys. Rev. B* **25**, 7661 (1982).
- ⁴⁸ V. Ranjan, G. Allan, C. Priester, and C. Delerue, *Physical Review B* **68**, 115305 (2003).
- ⁴⁹ M. Zielinski, W. Jaskolski, J. Aizpurua, and G. W. Bryant, *Acta Physica Polonica A* **108**, 929 (2005).
- ⁵⁰ S. Schulz, S. Schumacher, and G. Czycholl, *Phys. Rev. B* **73**, 245327 (2006).
- ⁵¹ E. Pelucchi, S. Watanabe, K. Leifer, B. Dwir, and E. Kapon, *Physica E* **23**, 476 (2004).
- ⁵² V. Dimastrodonato, E. Pelucchi, and D. D. Vvedensky, *Phys. Rev. Lett.* **108**, 256102 (2012).
- ⁵³ G. Juska, V. Dimastrodonato, L. O. Mereni, T. H. Chung, A. Gocalinska, E. Pelucchi, B. V. Hattem, M. Ediger, and P. Corfdir, *Phys. Rev. B* **89**, 205430 (2014).
- ⁵⁴ A. Joshi, *Elements of Group Theory for Physicists* (New Age International, 1997).
- ⁵⁵ G. L. Bir and G. E. Pikus, *Sov. Phys. Solid State* **3**, 2221. [*Fiz. Tverd. Tela (Leningrad)*, 1961, **3**, 3050] (1962), [*Fiz. Tverd. Tela (Leningrad)*, 1961, **3**, 3050].
- ⁵⁶ H. R. Trebin, U. Rössler, and R. Ranvaud, *Phys. Rev. B* **20**, 686 (1979).
- ⁵⁷ M. Silver, W. Batty, A. Ghiti, and E. P. O'Reilly, *Phys. Rev. B* **46**, 6781 (1992).
- ⁵⁸ O. Stier, M. Grundmann, and D. Bimberg, *Phys. Rev. B* **59**, 5688 (1999).
- ⁵⁹ L. W. Wang, A. J. Williamson, A. Zunger, H. Jiang, and J. Singh, *Applied Physics Letters* **76** (2000).
- ⁶⁰ O. Marquardt, D. Mourad, S. Schulz, T. Hickel, G. Czycholl, and J. Neugebauer, *Phys. Rev. B* **78**, 235302 (2008).
- ⁶¹ G. Juska, V. Dimastrodonato, L. Mereni, A. Gocalinska, and E. Pelucchi, *Nanoscale Research Letters* **6**, 567 (2011).
- ⁶² S. Schulz, D. P. Tanner, E. P. O'Reilly, M. A. Caro, T. L. Martin, P. A. J. Bagot, M. P. Moody, F. Tang, J. T. Griffiths, F. Oehler, M. J. Kappers, R. A. Oliver, C. J. Humphreys, D. Sutherland, M. J. Davies, and P. Dawson, *Phys. Rev. B* **92**, 235419 (2015).
- ⁶³ S. Schulz, M. A. Caro, and E. P. O'Reilly, *Applied Physics Letters* **104**, 172102 (2014).
- ⁶⁴ S. Schulz, M. A. Caro, C. Coughlan, and E. P. O'Reilly, *Phys. Rev. B* **91**, 035439 (2015).
- ⁶⁵ A. Schliwa, M. Winkelnkemper, and D. Bimberg, *Phys. Rev. B* **79**, 075443 (2009).
- ⁶⁶ A. Franceschetti and A. Zunger, *Phys. Rev. Lett.* **78**, 915 (1997).
- ⁶⁷ A. Franceschetti, L. W. Wang, H. Fu, and A. Zunger, *Phys. Rev. B* **58**, R13367 (1998).
- ⁶⁸ M. Rohlfing and S. G. Louie, *Phys. Rev. B* **62**, 4927 (2000).
- ⁶⁹ M. Wimmer, S. V. Nair, and J. Shumway, *Phys. Rev. B* **73**, 165305 (2006).
- ⁷⁰ M. Winkelnkemper, A. Schliwa, and D. Bimberg, *Phys. Rev. B* **74**, 155322 (2006).
- ⁷¹ C. Kindel, S. Kako, T. Kawano, H. Oishi, Y. Arakawa, G. Hönl, M. Winkelnkemper, A. Schliwa, A. Hoffmann, and D. Bimberg, *Phys. Rev. B* **81**, 241309 (2010).
- ⁷² S. Schulz, S. Schumacher, and G. Czycholl, *Phys. Rev. B* **73**, 245327 (2006).
- ⁷³ R. Benchamekh, F. Raouafi, J. Even, F. Ben Cheikh Larbi, P. Voisin, and J.-M. Jancu, *Phys. Rev. B* **91**, 045118 (2015).
- ⁷⁴ M. Korkusinski, O. Voznyy, and P. Hawrylak, *Phys. Rev. B* **84**, 155327 (2011).
- ⁷⁵ S. Richard, F. Aniel, and G. Fishman, *Phys. Rev. B* **70**, 235204 (2004).
- ⁷⁶ L. C. Lew Yan Voon and L. R. Ram-Mohan, *Phys. Rev. B* **47**, 15500 (1993).